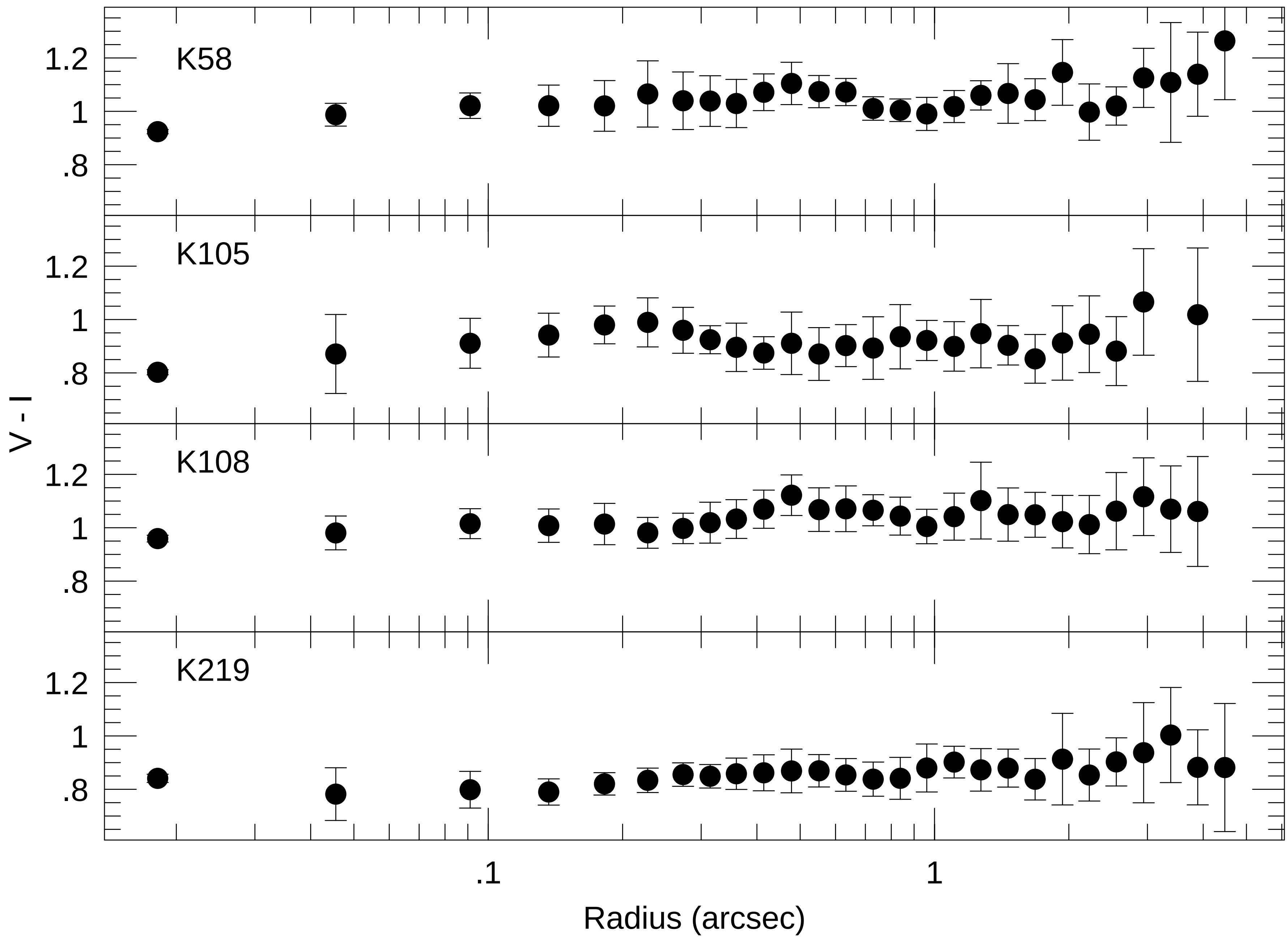

K58
K105
K108
K219
1.2
1
.8
V - I
.1
1
Radius (arcsec)

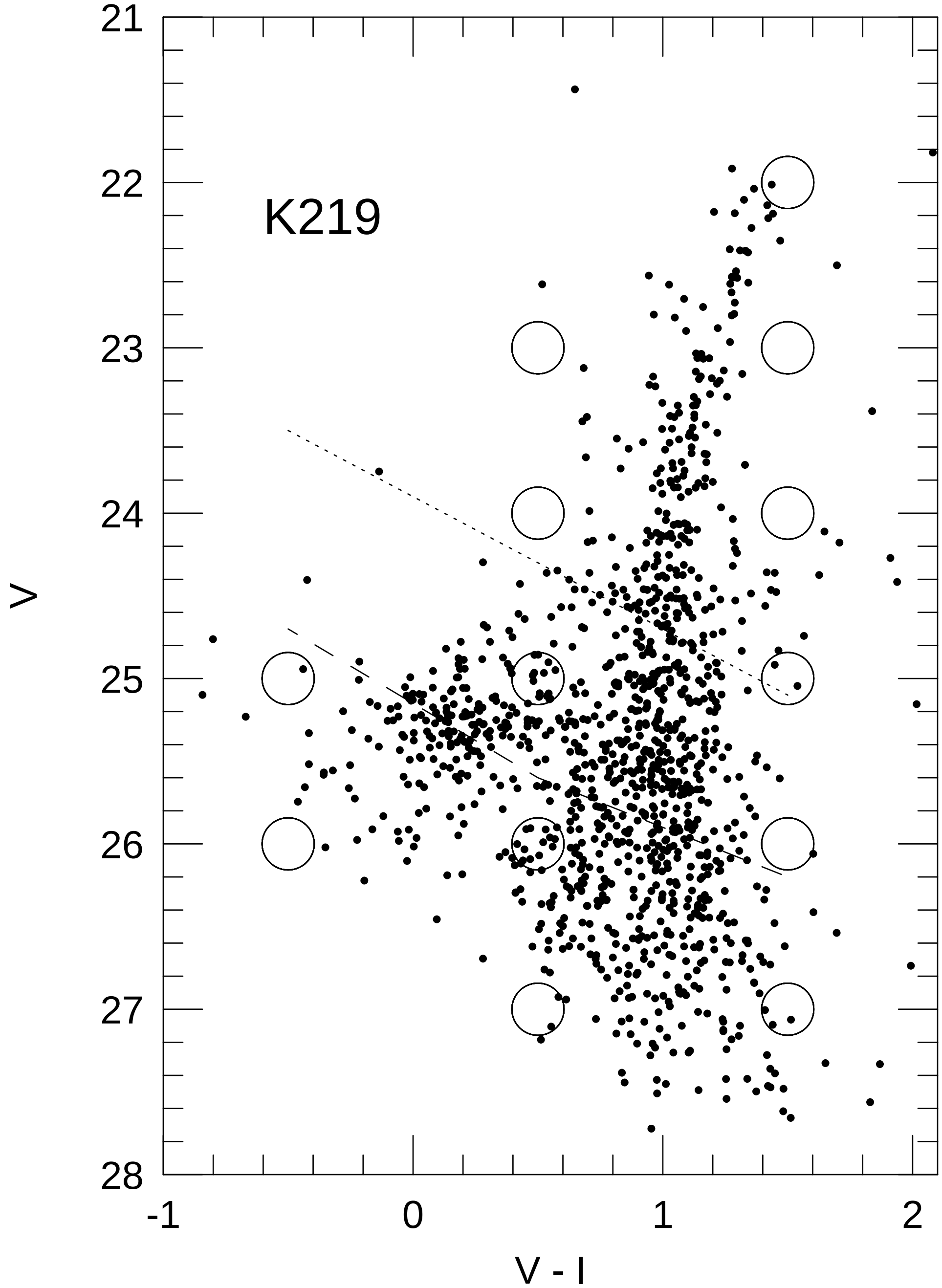

K219
V
V - I
21
22
23
24
25
26
27
28
-1
0
1
2

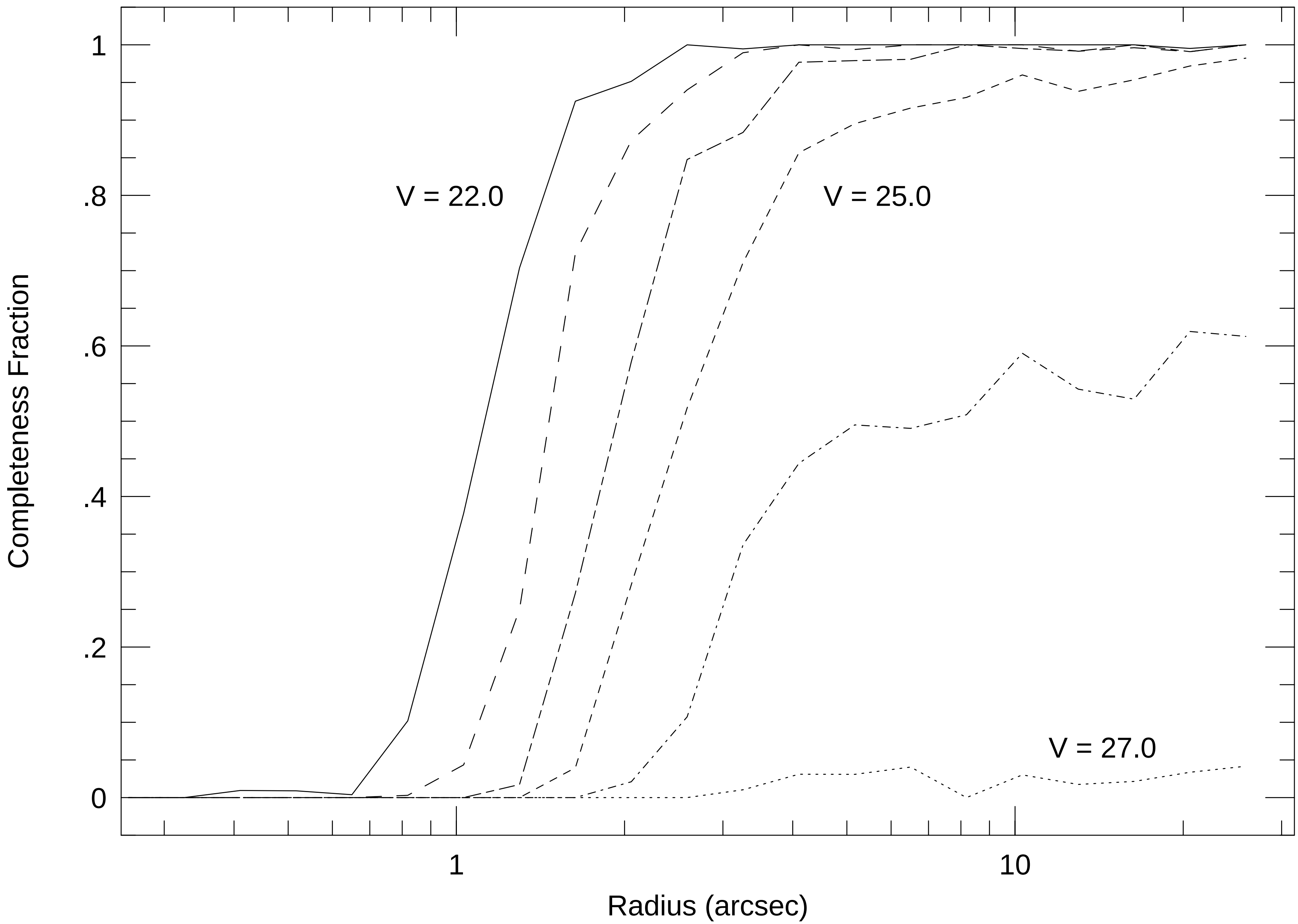
V = 22.0
V = 25.0
V = 27.0
Completeness Fraction
1
.8
.6
.4
.2
0
1
10
Radius (arcsec)

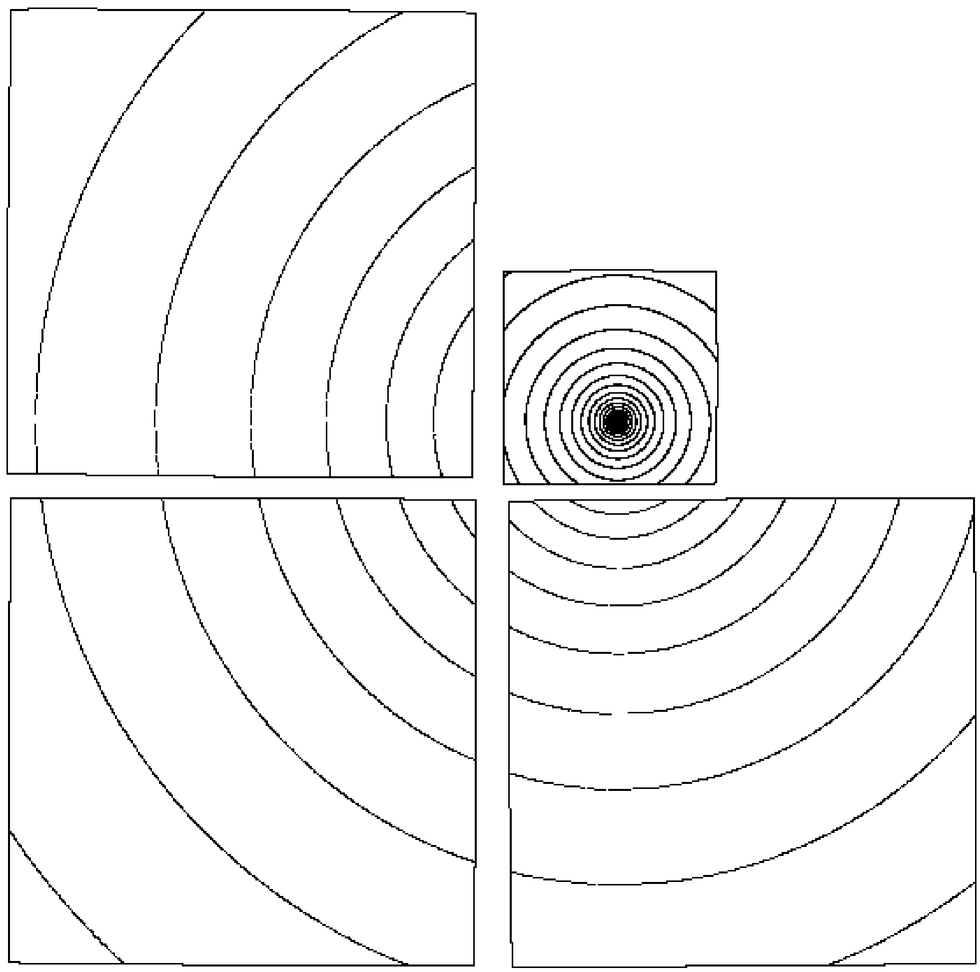

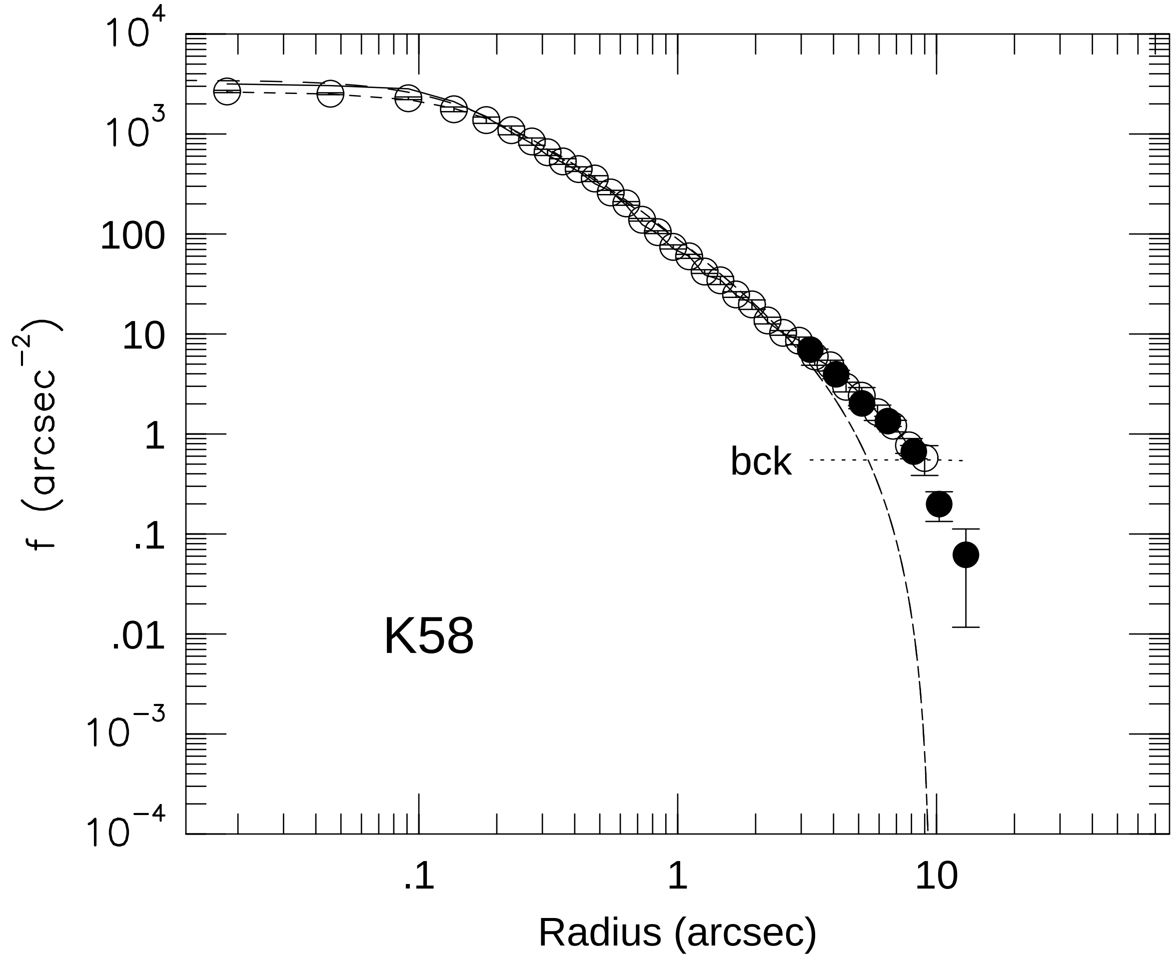

10^4
10^3
100
10
1
.1
.01
10^{-3}
10^{-4}
f (arcsec^{-2})
bck
K58
.1
1
10
Radius (arcsec)

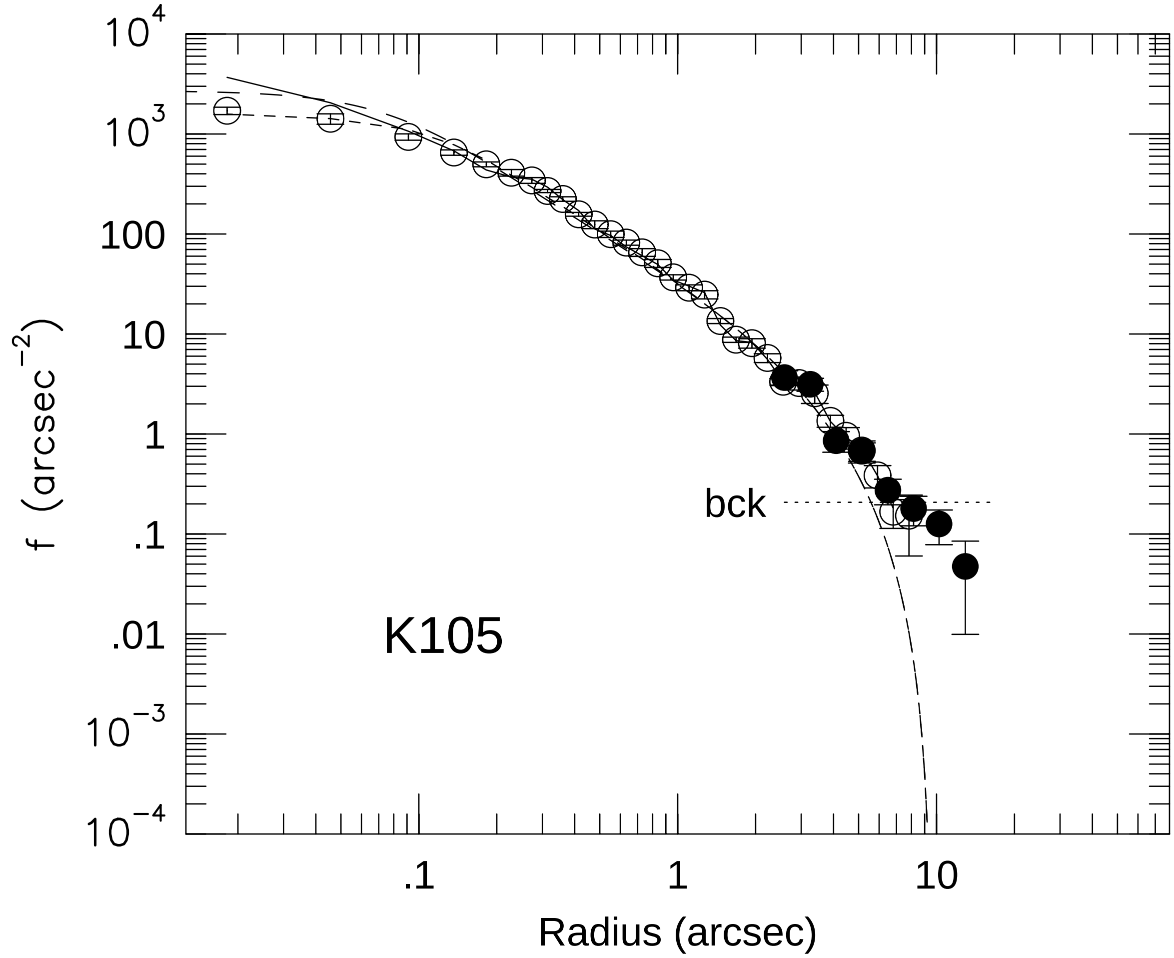

10^4
10^3
100
10
1
.1
.01
10^{-3}
10^{-4}
f (arcsec^{-2})
bck
K105
.1
1
10
Radius (arcsec)

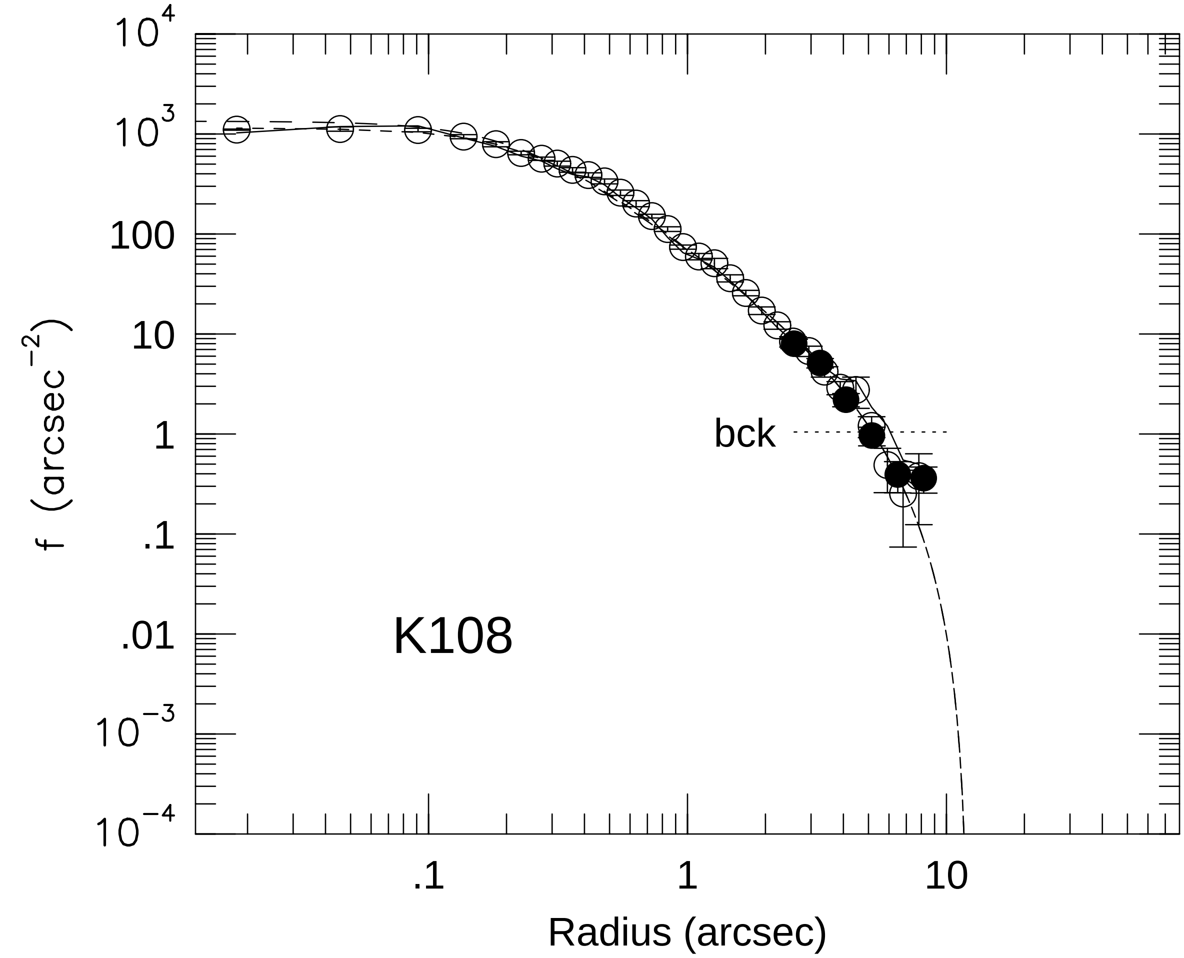

10^4
10^3
100
10
1
.1
.01
10^{-3}
10^{-4}
f (arcsec^{-2})
bck
K108
.1
1
10
Radius (arcsec)

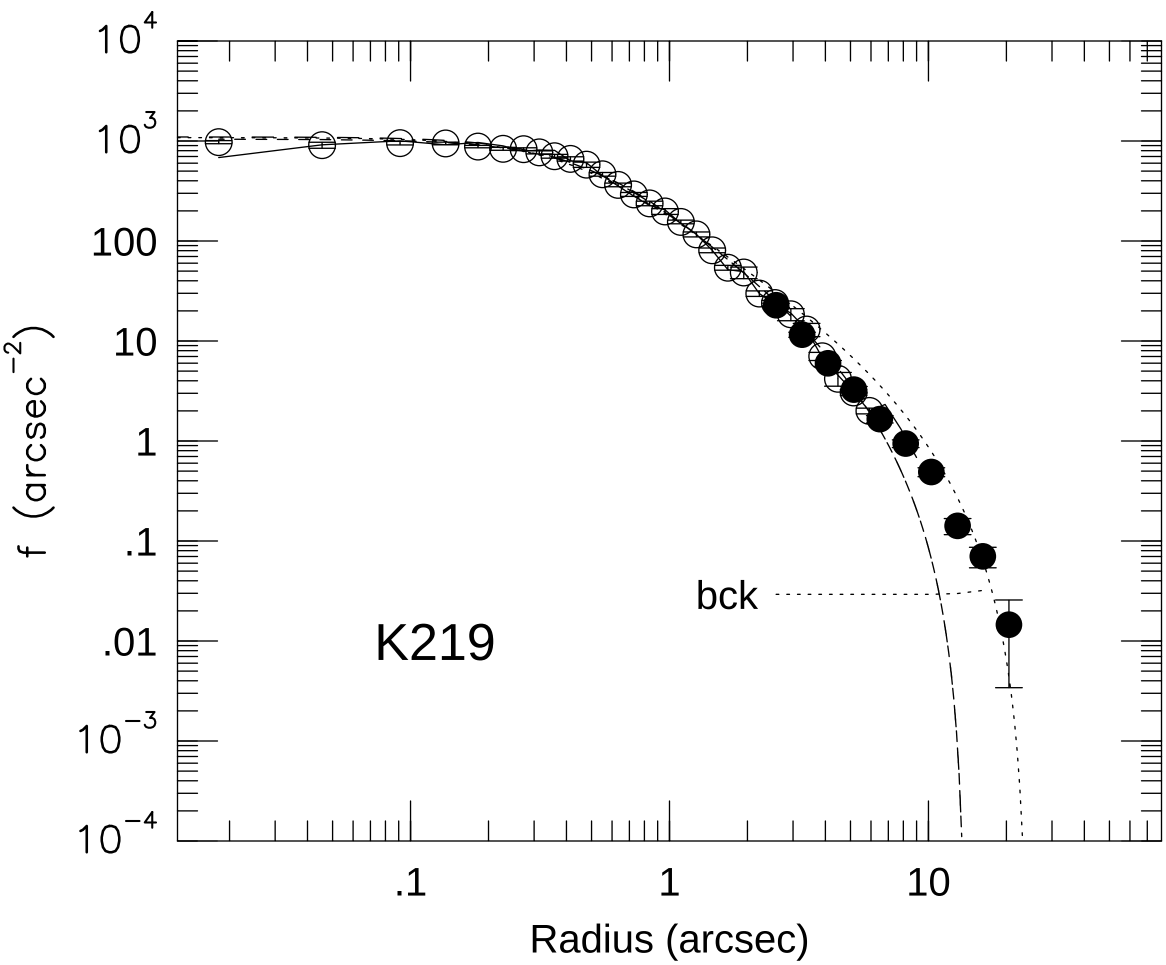

f (arcsec^{-2})
10^4
10^3
100
10
1
.1
.01
10^{-3}
10^{-4}
bck
K219
.1
1
10
Radius (arcsec)

Hubble Space Telescope Observations of Globular Clusters in M31 II: Structural Parameters[1]

Carl J. Grillmair[2]
UCO/Lick Observatory, University of California, Santa Cruz, CA 95064

Edward A. Ajhar
KPNO, National Optical Astronomy Observatories [3], P.O.Box 26732, Tucson, AZ 85726

Sandra M. Faber
UCO/Lick Observatory, Board of Studies in Astronomy and Astrophysics, University of California, Santa Cruz, CA 95064

William A. Baum
University of Washington, Astronomy Department, Box 351580, Seattle, WA 98195

Jon A. Holtzman
Astronomy Department, New Mexico State University, Box 30001 / Dept. 4500, Las Cruces, NM 88003

Tod R. Lauer, C. Roger Lynds, and Earl J. O'Neil, Jr.
KPNO, National Optical Astronomy Observatories[3], P.O.Box 26732, Tucson, AZ 85726

ABSTRACT

We analyze post-refurbishment Hubble Space Telescope images of four globular clusters in M31. The ability to resolve stars to below the horizontal branch permits us to use star counts to extend the surface brightness profiles determined using aperture photometry to almost 5 orders of magnitude below the central surface density. Three of the resulting cluster profiles are reasonably well-fit using single-mass King models, with core and tidal radii typical of those seen in Galactic globular clusters. We confirm an earlier report of the discovery of a cluster which has apparently undergone core collapse. Three of the four clusters show departures in their outskirts from King model behavior which, based on recent results for Galactic globulars, may indicate the presence of tidal tails.

[1]Based on observations with the NASA/ESA Hubble Space Telescope, obtained at the Space Telescope Science Institute, which is operated by AURA, Inc., under NASA contract NAS 5-26555.

[2]Current Address: Jet Propulsion Laboratory, California Institute of Technology, Mail Stop 183-900, 4800 Oak Grove Drive, Pasadena, CA 91109-8099

[3]Operated by AURA under cooperative agreement with the National Science Foundation.

Subject headings: globular clusters: general – galaxies: star clusters – galaxies: structure

1. Introduction.

Globular clusters have been and continue to be useful tools in the study of the structure, formation, dynamics, and distances of galaxies. The clusters themselves are dynamically simple systems, and are sufficiently luminous to be visible out to $cz \approx 10000$ km/sec (Harris 1991). Much recent work has concentrated on the degree to which the properties of globular clusters differ from one galaxy to the next. For example, an important issue currently being addressed is whether the globular cluster luminosity function and its peak are sensitive to metallicity (*e.g.* Ashman *et al.* 1995), and observably different for early- and late-type galaxies. Considerable work is being done to better understand the physical processes which would alter the structure and dynamics of individual clusters, and thereby the global properties of globular cluster *systems*. For example, different orbit shapes, tidal fields, and the presence of disks and bulges may have profound consequences for the ultimate survival of individual clusters, and for the constitution of cluster systems as a whole (Chernoff & Weinberg 1990; Kundic & Ostriker 1995). While hypotheses are in abundance, the observations necessary to test these ideas remain rather sparse. We need to make detailed studies of globular clusters in differing environments if we are to put useful constraints on the models.

The surface brightness profiles of most globular clusters in our own Galaxy have long been known to be reasonably well represented by King models (King 1966), which require the minimum possible number of parameters to describe the central density, total energy, and external tidal field. Together, the measured core or half-light radii and central densities yield information concerning the formation and long-term dynamical evolution of individual clusters. Conversely, the limiting radii are sensitive, on a relatively short time scale, to the influence of external potentials. The actual form of the observed tidal "cutoff" is determined by cluster mass, the tidal field of the galaxy, and the shape and phase of the cluster orbit (Oh and Lin 1992; Grillmair *et al.* 1996). While these quantities are not well constrained for any one cluster, obtaining information on a large sample of clusters should enable us to describe the mean orbital properties of the ensemble, as well as to map the potential of the host galaxy. M31 globular clusters are especially interesting in this respect because (*i*) the M31 cluster system is the most populous cluster system in the Local Group, (*ii*) we observe the cluster system from a vantage point outside the system, and (*iii*) M31 is similar in many respects to our own Galaxy, permitting us to gauge the sensitivity of globular cluster

properties to detailed structural differences.

The superb resolution afforded by the Hubble Space Telescope (HST) since the installation of the Wide Field/Planetary Camera-2 (WFPC-2) permits study of the stellar content and distribution in extragalactic globular clusters at a level of detail hitherto only possible for clusters belonging to our own Galaxy and its satellites. The observations discussed below were motivated primarily by a desire to calibrate the metallicity dependence of horizontal branch (HB) magnitudes (Ajhar *et al.* 1994; Ajhar *et al.* 1996, hereafter Paper I). However, the spatial resolution and the depth of the observations also allow a detailed examination of the structure of the clusters themselves. The mass/luminosity ratios derived from velocity dispersion measurements of our sample clusters are discussed elsewhere (Dubath and Grillmair 1996).

Section 2 briefly summarizes the observations. Section 3 describes synthetic aperture photometry, and a star-count analysis is carried out in Section 4. We present the results and discuss their implications in Section 5, and briefly summarize our findings in Section 6.

2. Observations.

As one of the primary motivations for HST imaging of globular clusters in M31 was to calibrate the metallicity dependence of horizontal branch (HB) magnitudes, the clusters we chose to observe were selected to give a wide range in metallicity and to be as clear of the disk of M31 as possible. The four clusters we examined are discussed in detail in Paper I, and we simply summarize the basic data concerning our targets in Table 1. Cluster designations refer to the list of Sargent *et al.* (1977) while magnitudes and metallicities are from Huchra *et al.* (1991).

The images we discuss were taken in February, 1994, shortly after the WFPC-2 was installed in the HST. Two 1000s exposures in each of F555W (V) and F814W (I) were taken of each cluster. The telescope was pointed so as to put the target clusters in the Planetary Camera (PC), giving $0.0455''$ per pixel (Holtzman *et al.* 1995a). The images were taken prior to the reduction in CCD operating temperature from $-77°$C to $-88°$C, and accordingly suffer from a somewhat larger number of hot pixels (that is, pixels with abnormally high dark current) than is presently the case. The majority of these were removed using maps of the hot pixels developed by the WFPC-2 team. As discussed in Paper I, the higher operating temperature also affects photometry, so a 0.05 magnitude offset was applied to the F814W zeropoint given in Holtzman *et al.* (1995b).

3. Aperture Photometry

Synthetic, concentric aperture photometry was carried out on both the F555W and F814W images. The centers of the clusters were determined by computing the center-of-light in circular annuli of varying radii (from 0.25-1.0″), and by subtracting fitted, 2-dimensional King models from the images. Aside from a few ~ 1 pixel excursions due to bright giants, the coordinates of center were found to be reasonably uniform with radius, and are accurate to within a pixel. Sky-background levels were estimated by computing the mean counts in regions lying as far as possible from the clusters. Owing to the large apparent size of the clusters in the PC, variations in the distribution of background sources, the presence of bright stars, and gradients due to the distribution of halo stars of M31, the uncertainty in sky-background levels is about 5%. Aperture photometry was carried out using a fixed center and circular apertures. The uncertainties were computed based on the spread in surface brightnesses measured in 8 sectors spread evenly around each annulus, combined in quadrature with the estimated uncertainty in the sky background. For the central pixel, the uncertainty was computed based on both photon statistics and centering errors. Our surface brightness measurements, transformed to V and I magnitudes using the coefficients of Holtzman *et al.* (1995b), corrected for reddening using the reddening law of DaCosta & Armandroff (1990),

$$A_V : A_I : E_{B-V} = 3.200 : 1.858 : 1.000, \tag{1}$$

and the values of E_{B-V} given in Paper I, are tabulated in Tables 2 through 5. We include only those radii for which the estimated uncertainties are less than 0.25 mag.

In Figure 1 we show the background-subtracted, $V-I$ color profiles of the four clusters. No significant color gradient is evident in any of the clusters, and the $\simeq 0.1$ mag bluing apparent at the smallest radii in K58 and K105 is consistent with scatter in the color distribution owing to the discrete distribution of the brightest (and reddest) stars in the cluster. However, this does not preclude the existence of a substantial number of blue stragglers in the cores of these clusters (which happen to be the two most concentrated in our sample).

Careful inspection of the images of K108 and division of the images by 2-dimensional King-model fits reveal what at first glance appears to be a very narrow dust lane. The lane crosses the cluster only 0.1″ from the center, extending $\simeq 1.5''$ in either direction. In some respects it resembles the rings of dust seen in HST images of the centers of elliptical galaxies (Grillmair *et al.* 1994; van Dokkum & Franx 1996)). On the other hand, K108 is projected only 22′ from the nucleus of M31, and a dust lane might better be attributed to the intervening ISM of M31's disk. Division of F555W by F814W reveals that the color

of the feature is actually slightly *bluer* than the surrounding starlight. This would suggest that, rather than caused by obscuration, the dimming is simply a consequence of a statistical dearth of red giant stars over a small region.

4. Star Counts

Owing to the low sky brightness in the WFPC-2 frames, the aperture photometry extends reliably for some considerable distance beyond the core radii of our clusters. However, at large radii the uncertainties become dominated by the distribution of relatively few, luminous giants. We consequently used star counts to enable us to extend the radial profiles to even lower surface densities.

Star counts were carried out using DAOPHOT II and ALLSTAR (Stetson 1987; 1994a). Initial experiments were conducted using the newer and more accurate ALLFRAME routine (Stetson 1994b), but owing to (*i*) the significantly increased amount of CPU time required to obtain a list of magnitudes and colors, (*ii*) the need for very extensive completeness tests (see below), and (*iii*) the similarity in the color-magnitude distributions of cluster and field stars (which ruled out separating cluster and field stars on the basis of color), we concluded that DAOPHOT/ALLSTAR were of themselves sufficient for our purposes.

Based on the sizes of globular clusters in the Milky Way, we expected that the tidal radii of our sample clusters would be of the same order as the field-of-view of the PC. Combined with the off-center locations of the clusters in the PC and the presence of a gradient in the surface density of field stars due to the halo of M31, we elected to include all four WFPC-2 chips in our analysis. Objects were detected and measured in the summed F555W and F814W images and the output detection lists were used to compute magnitudes and colors using the WFPC-2 zeropoints and color terms of Holtzman *et al.* (1995b). Examination of images from which the measured stars had been subtracted revealed that residual cosmic rays, visibly warm pixels, and extended objects had, in the vast majority of cases, been so identified and subsequently ignored by the software. We estimate that less than 1% of objects classified by DAOPHOT as stars could with some degree of confidence be called galaxies, cosmic rays, or hot pixels. Using the point spread function (PSF) index described by Baum *et al.* (1995) we find that, at our ultimately selected magnitude cutoff of $V = 25.5$, we are well clear of the regime where spurious detections become significant. Only stars having both an F555W and an F814W measurement and colors and magnitudes reasonably consistent with those of cluster stars were counted. However, since the background is overwhelmingly dominated by stars in the halo of M31 (whose distribution over apparent magnitude and color is almost identical to that of the cluster stars), little differentiation is possible.

The detection and measurement of individual stars becomes progressively more difficult as one approaches the crowded, inner regions of each cluster. For the PC images, magnitudes were consequently measured using the crowded-field, PSF-fitting code ALLSTAR. On the other hand, owing to the relatively uncrowded nature of the outer fields, combined with the higher degree of undersampling (making PSF-fitting problematic), magnitudes of sources detected in the WF chips were measured using simple aperture photometry. Naturally, the use of two different measuring algorithms, combined with spatially varying noise and crowding levels, differing pixel-scales, and zero-point offsets between chips, meant that extensive simulations were required to combine the various star-count results and surface brightness measurements reliably.

The probability of detecting a particular star varies with radius, magnitude, color, and chip number. Completeness tests were carried out by adding appropriately scaled PSFs to the images and running the DAOPHOT II/ALLSTAR detection and measuring routines in a manner identical to that applied to the real data. We divided the color-magnitude diagrams into a 1×1 magnitude grid as shown in Figure 2. Experiments were conducted independently for each cluster, each chip, and each color-magnitude bin, and typically 200 artificial stars were added in the course of each experiment. Artificial stars with a specified V magnitude were added to the F555W frame, and a matching set of stars with identical, cluster-centric coordinates and I-magnitudes appropriate to the specified color were added to the F814W frame. The DAOPHOT II/ALLSTAR sequence was applied to both frames, and the output photometry files were compared to determine how many artificial stars were retrieved in both frames. Account was also taken of changes in magnitude due to the overlaying of artificial stars onto natural stars; the completeness fraction in the brighter magnitude bin was increased accordingly. To reduce the Poisson uncertainties in the derived completeness fractions, between 5 and 10 completeness experiments were conducted in this manner for each color-magnitude bin. Thus, our derived completenesses for each chip and each color-magnitude bin derive from between 1000 and 2000 simulated stars. In total, $\sim 10^5$ artificial stars were added for each cluster.

The artificial stars were distributed in such a manner that the local surface density was increased by no more than 5% over its natural value. Consequently, the distribution of added stars as a function of radius resembled the King-like profiles of the underlying cluster surface density distributions, with most of the stars being added to the central regions where incompleteness is most severe. Artificial stars were added eight at a time to each annular bin, equally spaced in position angle but with random phase differences (extending to sub-pixel scales) between successive radial bins and from one simulation to the next. The completeness fraction as a function of radius and magnitude at a fixed color for the PC frame of K219 is shown in Figure 3.

Star counts were carried out in logarithmically-spaced, annular bins as shown in Figure 4. For each star counted, the completeness appropriate to its radius, magnitude, and color was estimated using the nearest completeness point in radius, and bilinear interpolation of the four nearest points in the color-magnitude grid. Each natural star of suitable color was then divided by the computed completeness fraction to obtain the actual surface density of stars in each annular bin. The positions of the detected stars and the areas encompassed by different annuli were computed using the distortion coefficients of Holtzman *et al.* (1995a). The counts were limited to stars with $V < 25.5$, this limit being chosen to give a reasonable degree of overlap with the aperture photometry results without requiring excessively large (*i.e.* more than a factor of five) completeness corrections. Roughly speaking, $V = 25.5$ corresponds to a completeness fraction of $\approx 50\%$ for red stars at a radius of $3''$.

4.1. Surface Density of Field Stars

Contamination of the star counts by field stars (the majority of which reside in the halo of M31) was not straightforward to estimate for three reasons: (*i*) the clusters were not centered in the PC field of view, (*ii*) the tidal radii of the sample clusters are similar in extent to the size of the PC frame, and (*iii*) some clusters are close enough to M31 that the spatial distribution of field stars is significantly nonuniform.

To determine the gradient in the surface density of field stars, we used DAOPHOT II to find and carry out aperture photometry of all objects in the WF frames. We found that, over the field of view of WFPC-2, the distribution of field stars does not depart significantly from a linear function of the x and y pixel position. Consequently, after applying the appropriate completeness corrections, we modeled the surface density z of field stars with a plane of the form

$$z = c_0 + c_1 x + c_2 y. \tag{2}$$

where the ratio c_1/c_2 was fixed by specifying the direction of the maximum gradient in the surface density of field stars. This direction was independently determined by using the Digitized Sky Survey to examine M31 isophotes local to each cluster. In addition to reducing the number of free parameters, defining the orientation of this plane in advance allowed us to more easily identify regions with anomalously high or low surface densities.

After masking regions obviously contaminated by galaxies, star clusters, or other localized enhancements, Equation 1 was individually fitted to the distributions in each of the three WF frames. The coefficients were then (*i*) averaged, (*ii*) scaled to match the pixel-scale

of the PC frame, and (*iii*) normalized to the surface density of stars measured in a $9'' \times 33''$ box on the side of the PC furthest removed from the center of the cluster. The ability to predict the density of field stars at arbitrary locations in the field enabled us to carry out star counts in annuli which were not complete due to the limited field-of-view of the PC. The raw star counts are given along with the annular areas, mean annular background level, average completeness corrections, and corrected surface densities in Tables 6 through 9.

5. Discussion

In Figures 5 through 8 we show the surface density profiles derived from both the star counts and the aperture photometry for each of the four clusters. The aperture photometry has been scaled to match the star counts in the region of overlap. The error bars plotted for the aperture photometry include a 0.3 DN uncertainty in the sky-background level, and the uncertainties for the inner two points have been set to half the difference in DN between them to account for possible miscentering. The error bars shown for the star counts take account of both Poisson statistics and the uncertainties in the completeness corrections. The data are shown only out to the radius at which the surface density first becomes consistent (within the computed error bar) with zero. The apparent agreement between the aperture photometry and the star counts in the region of overlap suggests that our estimates of the sky background are not grossly in error.

Shown as solid lines in Figures 5 through 8 are the results of 20 deconvolution iterations using the Lucy-Richardson (Richardson 1972; Lucy 1974) algorithm. Simulations have shown that deconvolution of WFPC-2 data to this extent permits reliable recovery of information down to $\approx 0.05''$. The deconvolved profiles of both K108 and K219 show a decline (relative to the "raw" profile) in the flux measured for the central pixel. This is due to the presence of one or more relatively bright red giants within a few pixels of the center. On the other hand, the inner deconvolved profile for K105 shows a general steepening and a factor of two increase in the flux measured in the central pixel. This is in agreement with the results of Bendinelli *et al.* (1993), who used deconvolved, pre-refurbishment Faint Object Camera (FOC) images to determine that K105 (G105 in their paper) has a power-law cusp at the center and has therefore likely undergone core collapse. Indeed, over the range $0.045'' \leq r \leq 0.23''$, we find a power-law slope of -1.08 ± 0.1, somewhat steeper than their estimated value of -0.75, and strongly suggestive of a past or impending gravothermal catastrophe.

The long-dashed and short-dashed lines in Figures 5 through 8 are the best-fitting, single-mass King models before and after 2-dimensional convolution with the PC PSF. King-model fitting was carried out in two stages; owing to significant coupling between r_c and r_t

and the apparent departures of the observations from King-like behavior at large radii (see below), we chose to fit core and tidal radii separately. Firstly, two-dimensional, single-mass King models were generated and convolved with the PSF appropriate to the position of the cluster on the PC (*e.g.* Lauer *et al.* 1991). The PSF itself was generated using DAOPHOT II to model the morphologies of the brightest ∼30 point sources in each frame. Aperture photometry, in a manner identical to that used for the real data, was carried out to produce a one-dimensional surface density profile, and this profile was then compared with the data to obtain a value of χ^2. Using a downhill-simplex method, the core radius and normalization constant were estimated using aperture photometry data within $1''$ of the center. Secondly, the tidal radius was estimated using both aperture photometry and star count data by fixing r_c and searching for the value of r_t which gave the minimum reduced χ^2. Our best-fit values for r_c and r_t were converted to spatial units assuming a distance to M31 of 770 kpc (Paper I) and are tabulated and compared with those of previous investigators in Table 10.

The uncertainties in the core and tidal radii were estimated using Monte Carlo simulations of the data, based on both the error bars shown in Figures 5 through 8 and a 5% uncertainty in the adopted sky brightness. Irrespective of departures from King-like behavior, the simulations yielded 90% confidence intervals of $\approx 1.2''$ (4.5pc) in r_t for all clusters. For K58 and K105, the 90% confidence intervals on r_c were $\approx 0.01''$ (0.04pc), and for K108 and K219 they were $\approx 0.02''$ (0.08pc). Of course, these uncertainties apply only in those cases where it is clear that a King model is appropriate. The power-law cusp in the deconvolved profile of K105, for example, is not well fit by the King model which best matches the raw data, and if there is indeed a constant surface brightness core in this cluster, it is likely to be considerably overestimated by the value of r_c given in Table 10. Similarly, the formal fitting uncertainties on r_t are largely irrelevant in those cases where there is a clear discrepancy between the form of the model and that of the data.

The values we obtain for the half-light radii are typical of those found in Milky Way globular clusters ($< r_h >= 4.2$pc, Djorgovski 1993). It is reassuring that the HST study of K58 by Fusi Pecci *et al.* (1994) using deconvolved Faint Object Camera images yields a measurement of the core radius which is in reasonable agreement with ours. On the other hand, the half-light radius found by these authors for K58 (2.1pc) is somewhat smaller than the value of 2.8pc we find here. We attribute this discrepancy to the very small field of view ($11''$) of the FOC in its $f/96$ mode. Given the extent of the surface density profile shown in Figure 5, it is quite probable that they overestimated the sky brightness, leading to an underestimate of the total light and extent of K58. Their value of $r_h = 2.4$pc for K105 (compared to our value of 2.9pc) is consistent with this hypothesis.

With the exception of K108 (which, in projection, lies closest to M31 and hence is

most severely affected by background uncertainties), all clusters show apparent departures from the best fitting King model at radii approaching r_t. These departures take the form of an excess of stars near and beyond the fitted r_t, and occur between 3 and 4 orders of magnitude below the central surface density. K105 and K219 illustrate this effect most dramatically. Both the star counts and the aperture photometry show a tidal turn-down beyond $1''$. However, rather than following the model profiles to a steep tidal-cutoff, the data continue downwards in a comparatively shallow, power-law fashion.

Due to the distribution of uncertainties, the best-fitting values of r_t are heavily influenced by the inner few data points derived from the star counts. The single-mass King models cannot be made to fit the extended portions of the profiles due to the characteristic, upward inflection of high-concentration, King model profiles. This is illustrated in Figure 8, where we have plotted a King model with core radius and normalization identical to that of the King model which best fits the data for K219, but with the tidal radius increased to $24''$ (90pc). Although this model passes through the outermost points, the reduced χ^2 is very much greater than for the best-fit case. Clearly, no renormalization of this extended model would improve the overall fit to the data.

Note that the cluster isophotes have ellipticities ranging from ~ 0.07 (K58) to ~ 0.18 (K219). However, even if we assumed that the tidal cutoff radius varies with position angle like the isophotes, the tidal radius measured along the major axis of the cluster should differ by no more than 10% from the tidal radius predicted by a circular model. The differences between the radius of the last measured, non-zero star count datum and the radius at the same surface density of the best-fitting King model exceed what one might have expected purely from cluster ellipticity by factors of ~ 8 (K219) to ~ 15 (K105). Moreover, K108 shows moderate isophote ellipticities (~ 0.12), but the star counts near r_t are well fit by a King model. Hence we conclude that the departures near r_t between the models and the star counts are not related to the ellipticities seen in the isophotes.

The departures from King models are consistent, both in magnitude and in form, with the findings of Grillmair *et al.* (1995), who studied a sample of 12 Galactic globular clusters. They concluded that these extended profiles result from stars which have been stripped from their parent clusters and are in the process of migrating outwards along the tidal tails. The power-law profiles seen in their sample were found to exhibit a variety of slopes, consistent with N-body models of clusters on eccentric orbits (Grillmair *et al.* 1996). The magnitude of the effect and the slope of the power-law profile are functions of orbital phase and viewing angle. Owing to the much smaller number of resolved cluster stars in the present work (due to the much brighter limiting absolute magnitude), the uncertainties in the counts near r_t are significantly larger than for the sample of Grillmair *et al.* (1995). Similarly, the very

small numbers of "extra-tidal" stars relative to the background preclude a study of their two-dimensional distribution. However, the systematic behavior of the profiles shown in Figures 5 through 8 is consistent with the conclusions reached by these authors.

One might be tempted to dismiss the foregoing on the grounds that single-mass King models must necessarily be too simplistic to adequately model the behavior of real clusters. However, we would argue that multi-mass King models are unlikely to be able to account for the observed profile shapes near r_t due to the very small range of stellar masses represented among the counted stars. Likewise, the aperture photometry is dominated by giant branch stars, so much so that stars with $V < 26.5$ (the regime sampled by the star counts) constitute $\approx 80\%$ of the total light from each cluster. We note that $\approx 50\%$ of the light is contributed by stars above the horizontal branch, while only $\approx 20\%$ of the completeness-corrected star counts occur above the same magnitude level. Nonetheless, the difference in mean stellar mass over this magnitude interval is entirely inconsequential from the standpoint of dynamical segregation.

K105 is somewhat analogous to M15 in having both a collapsed core and a pronounced excess of extra-tidal stars. That both phenomena should be observed in each of these clusters may not be surprising; the early onset of core collapse and a rapid rate of repopulation of the tidally stripped region of a cluster both rely on a relatively short 2-body relaxation time.

6. Summary

We have analyzed WFPC-2 images of four globular clusters associated with M31 to obtain surface density profiles and structural parameters. Using aperture photometry and star count analyses, we find that:

- there is no evidence for color gradients in the aperture photometry,
- for three of the clusters the inner portions of the 1-dimensional surface density profiles can be reasonably-well modeled using single-mass King models,
- we confirm the discovery by Bendinelli that K105 is likely to have undergone core collapse, and
- for three of the clusters the surface density profiles depart from King models at large r in a manner which suggests the presence of tidal tails.

The detections of a collapsed core and possibly of tidal tails in extragalactic globular clusters are yet more tributes to the capabilities of HST. Since proper-motion studies are

unlikely to yield much useful information in the near future for globular clusters in M31, a deep study of the tidal tails may be the only way to expand our knowledge of the shapes of the cluster orbits. This in turn would enable us to infer the distribution of mass in M31's halo, and perhaps to answer some of the lingering questions concerning the origins of globular clusters and the formation and evolution of spiral galaxies.

This research was conducted by the WF/PC Investigation Definition Team, supported in part by NASA Grant No. NAS5-1661.

REFERENCES

Ajhar, E.A., Lauer, T.R., Lynds, C.R., O'Neil, E.J., Faber, S.M., Baum, W.A., Ewald, S.P., Grillmair, C.J., Light, R.M., & Holtzman, J.A. 1994 BAAS, 26, 938

Ajhar, E.A., Lauer, T.R., Lynds, C.R., O'Neil, E.J., Faber, S.M., Baum, W.A., Ewald, S.P., Grillmair, C.J., Light, R.M., & Holtzman, J.A. 1996, in preparation.

Ashman, K.M., Conti, A., & Zeph, S.E. 1995, AJ, in press.

Battistini, P., Bonoli, F., Buonanno, R., Corsi, C.E., & Fusi Pecci, F., 1982, A&A, 113, 39

Baum, W.A., Hammergren, M., Groth, E.J., Ajhar, E.A., Lauer, T.R., O'Neil, E.J., Lynds, C.R., Faber, S.M., Grillmair, C.J., Holtzman, J.A., & Light, R.M. 1995, AJ, in press.

Bendinelli, O., Cacciari, C., Djorgovski, S., Federici, L., Ferraro, F.R., Fusi Pecci, F., Parmeggiani, G., Weir, N., & Zavatti, F. 1993, ApJ, 409, L17

Chernoff, D.F., & Weinberg, M.D. 1990, ApJ, 372, 487

Cohen, J.G., & Freeman, K.C. 1991, AJ, 101, 483

Crampton, D., Schade, D.J., Chayer, P., & Cowley, A.P. 1985, ApJ, 288, 494

DaCosta, G.S., & Armandroff, T.E. 1990, AJ, 100, 162

Djorgovski, S. 1993, in *Structure and Dynamics of Globular Clusters*, p. 373, S.Djorgovski & G. Meylan (eds.), ASPCS vol. 50

Dubath, P., & Grillmair, C.J. 1996, in preparation.

Fusi Pecci, F., Battistini, P., Bendinelli, O., Bonoli, F., Cacciari, C., Djorgovski, S., Federici, L., Ferraro, F.R., Parmeggiani, G., Weir, N., & Zavatti, F. 1994, A&A, 284, 349

Grillmair, C.J., Faber, S.M., Lauer, T.R., Baum, W.A., Lynds, C.R., O'Neil, E.J. Jr., & Shaya, E.J. 1994, AJ, 108, 102

Grillmair, C.J., Freeman, K.C., Irwin, M., & Quinn, P.J. 1994, AJ, 109, 2553

Grillmair, C.J., Quinn, P.J.,Freeman, K.C., Fullagar, D. & Salmon, J. 1996, in preparation.

Harris, W.E. 1991, ARA&A, 29, 543

Holtzman *et al.* 1995a, submitted.

Holtzman, J.A., Burrows, C.J., Casertano, S., Hester, J.J., Trauger, J.T., Watson, A.M., & Worthey, G. 1995b, submitted.

Huchra, J.P., Kent, S.M., & Brodie, J.P. 1991, ApJ, 370, 495

King, I.R. 1966, AJ, 71, 64

Kundic, T., & Ostriker, J.P. 1995, ApJ, 438, 702

Lauer, T.R., Holtzman, J.A., Faber, S.M., Baum, W.A., Currie, D.G., Ewald, S.P., Groth, E.J., Hester, J.J., Kelsall, T., Light, R.M., Lynds, C.R., O'Neil, E.J., Schneider, D.P., Shaya, E.J., Westphal, J.A. 1991, ApJ, 369, L45

Lucy, L. B. 1974, AJ, 79, 745

Oh, K.S., & Lin, D.N.C. 1992, ApJ, 386, 519

Richardson, W. H. 1972, *J. Opt. Soc. A.*, 62, 52

Sargent, W.L., Kowal, C.T., Hartwick, F.D.A., & van den Bergh, S. 1977, AJ, 82, 947

Stetson, P. 1987, PASP, 99, 191

Stetson, P.B. 1994a, DAOPHOT II User's Manual

Stetson, P.B. 1994b, PASP, 106, 250

van Dokkum, P.G., & Franx, M. 1995, preprint.

This preprint was prepared with the AAS LaTeX macros v4.0.

Fig. 1.— $V-I$ Color profiles for the four clusters in our sample. The error bars reflect both the scatter among 8 sectors within each annulus, and the effect of a 0.3 DN uncertainty in the sky background.

Fig. 2.— Color-magnitude diagram of K219. The open circles show the points at which completeness simulations were carried out. The dotted line shows the colors and magnitudes corresponding to the 50% completeness level at a radius of $2.6''$ from the center of K219. Similarly, the dashed line indicates the 50% completeness level at a radius of $20''$.

Fig. 3.— Completeness fractions as a function of both radius and magnitude, determined from simulations using the PC images of K219. Shown here are the results for artificial stars of $V-I=1.5$.

Fig. 4.— Division of the WFPC-2 into annular and partial annular bins. Though not obvious on this scale, the annuli shown do take into account the field distortions induced by the camera optics. The gaps apparent between frames result from having uniformly excluded the first 60 x and y pixels in each chip so as to remain well clear of the pyramid shadow.

Fig. 5.— Surface density as a function of radius computed from the aperture photometry and star counts for K58. The open circles show the aperture photometry, scaled to match the star counts in the region of overlap. The filled circles are completeness-corrected surface densities derived from the star counts and are shown only out to the radius at which the background-subtracted surface density first becomes consistent with zero (to within the uncertainties). The solid line shows the aperture photometry after 20 Lucy-Richardson deconvolution iterations. The long-dashed line corresponds to the best-fitting King model (with parameters taken from Table 10), and the short-dashed line shows the same model after convolution with the WFPC-2 PSF.

Fig. 6.— Same as Figure 5, but for K105.

Fig. 7.— Same as Figure 5, but for K108.

Fig. 8.— Surface density as a function of radius computed using aperture photometry and star counts in K219. Symbols are as in Figure 5. In addition, the dotted line shows a King model with the same core radius and normalization as the solid line, but with a tidal radius increased to $24''$ so as to pass through the outermost, non-zero data points.

TABLE 1. Basic Data.

Cluster	α (2000)	δ	V	[Fe/H]
K58	0 40 26.8	+41 27 27.7	15.80	-0.57 ± 0.15
K105	0 41 42.2	+40 12 22.8	16.35	-1.49 ± 0.17
K108	0 41 43.3	+41 34 20.8	15.80	-0.94 ± 0.27
K219	0 43 18.0	+39 49 13.5	15.10	-1.83 ± 0.22

Table 2. K58 Aperture Photometry.

r	μ_V		μ_I	
$0\farcs018$	14.537 ±	0.006	13.616 ±	0.006
0.046	14.657	0.036	13.672	0.023
0.091	14.804	0.035	13.785	0.033
0.137	15.079	0.052	14.060	0.057
0.182	15.349	0.057	14.331	0.076
0.228	15.645	0.067	14.582	0.104
0.273	15.902	0.064	14.865	0.087
0.314	16.171	0.058	15.134	0.075
0.360	16.391	0.059	15.363	0.068
0.414	16.624	0.040	15.555	0.056
0.478	16.893	0.037	15.790	0.070
0.551	17.211	0.029	16.139	0.053
0.633	17.483	0.024	16.413	0.045
0.729	17.830	0.030	16.822	0.032
0.838	18.134	0.025	17.132	0.034
0.961	18.489	0.037	17.500	0.050
1.107	18.752	0.035	17.736	0.049
1.271	19.174	0.031	18.117	0.046
1.462	19.401	0.056	18.336	0.097
1.680	19.730	0.039	18.689	0.068
1.935	20.082	0.050	18.938	0.112
2.222	20.334	0.067	19.339	0.081
2.555	20.667	0.041	19.649	0.059
2.942	20.969	0.060	19.846	0.093
3.384	21.345	0.127	20.239	0.186
3.889	21.597	0.089	20.460	0.130
4.472	22.260	0.182	20.998	0.127
5.141	22.343	0.146	21.220	0.213
5.916	22.753	0.181	21.631	0.198
6.799	23.077	0.204	21.971	0.186

Table 3. K105 Aperture Photometry.

r	μ_V		μ_I	
$0\farcs018$	14.966 ±	0.007	14.165 ±	0.007
0.046	15.233	0.083	14.363	0.123
0.091	15.727	0.054	14.817	0.076
0.137	16.147	0.050	15.206	0.065
0.182	16.480	0.039	15.501	0.059
0.228	16.699	0.046	15.711	0.079
0.273	16.862	0.050	15.904	0.070
0.314	17.092	0.036	16.169	0.039
0.360	17.264	0.072	16.369	0.055
0.414	17.626	0.040	16.752	0.046
0.478	17.917	0.070	17.008	0.093
0.551	18.119	0.062	17.250	0.077
0.633	18.360	0.048	17.459	0.062
0.729	18.595	0.072	17.703	0.093
0.838	18.910	0.074	17.976	0.095
0.961	19.248	0.039	18.327	0.064
1.107	19.485	0.060	18.587	0.071
1.271	19.705	0.083	18.759	0.098
1.462	20.322	0.040	19.419	0.062
1.680	20.739	0.063	19.887	0.067
1.935	20.885	0.082	19.974	0.113
2.222	21.286	0.095	20.342	0.108
2.555	21.819	0.093	20.938	0.090
2.942	22.033	0.124	20.968	0.157
3.384	22.272	0.172	21.225	0.214
3.889	22.932	0.180	21.915	0.176

Table 4. K108 Aperture Photometry.

r	μ_V		μ_I	
0''018	15.507 ±	0.010	14.550 ±	0.009
0.046	15.513	0.036	14.535	0.052
0.091	15.572	0.037	14.559	0.042
0.137	15.730	0.037	14.725	0.050
0.182	15.925	0.046	14.913	0.062
0.228	16.112	0.038	15.133	0.044
0.273	16.272	0.040	15.277	0.040
0.314	16.415	0.048	15.398	0.059
0.360	16.587	0.047	15.556	0.056
0.414	16.752	0.045	15.685	0.056
0.478	16.962	0.047	15.843	0.060
0.551	17.191	0.049	16.125	0.065
0.633	17.467	0.045	16.398	0.073
0.729	17.774	0.036	16.711	0.046
0.838	18.077	0.043	17.036	0.057
0.961	18.488	0.040	17.486	0.051
1.107	18.762	0.044	17.722	0.077
1.271	18.989	0.078	17.890	0.121
1.462	19.312	0.052	18.265	0.085
1.680	19.680	0.053	18.634	0.066
1.935	20.093	0.037	19.073	0.092
2.222	20.452	0.062	19.443	0.091
2.555	20.907	0.078	19.847	0.124
2.942	21.199	0.081	20.085	0.125
3.384	21.667	0.107	20.599	0.131
3.889	22.060	0.140	21.001	0.166
4.472	22.479	0.171	21.061	0.328

Table 5. K219 Aperture Photometry.

r	μ_V		μ_I	
0.″018	16.055 ±	0.012	15.215 ±	0.011
0.046	16.073	0.067	15.292	0.073
0.091	16.038	0.053	15.241	0.044
0.137	16.038	0.036	15.249	0.033
0.182	16.146	0.030	15.327	0.029
0.228	16.215	0.029	15.382	0.035
0.273	16.245	0.027	15.391	0.035
0.314	16.319	0.023	15.471	0.037
0.360	16.425	0.036	15.568	0.046
0.414	16.494	0.042	15.634	0.053
0.478	16.646	0.051	15.778	0.064
0.551	16.887	0.041	16.019	0.045
0.633	17.137	0.042	16.284	0.045
0.729	17.359	0.043	16.522	0.048
0.838	17.587	0.056	16.747	0.055
0.961	17.826	0.056	16.947	0.070
1.107	18.110	0.039	17.209	0.045
1.271	18.393	0.052	17.521	0.060
1.462	18.798	0.042	17.919	0.057
1.680	19.192	0.051	18.355	0.059
1.935	19.385	0.105	18.473	0.135
2.222	19.853	0.070	19.001	0.067
2.555	20.138	0.059	19.237	0.068
2.942	20.454	0.124	19.518	0.141
3.384	20.900	0.089	19.898	0.154
3.889	21.449	0.096	20.568	0.101
4.472	22.012	0.172	21.131	0.165
5.141	22.327	0.098	21.473	0.099
5.916	22.760	0.123	21.935	0.123

Table 6. K58 Star Counts.

r_{inner} arcsec	r_{outer} arcsec	r arcsec	area arcsec^2	N	f_{bkd} arcsec^{-2}	α_c	f arcsec^{-2}	
2.277	2.867	2.582	9.5	85	0.550	1.758	15.146	1.012
2.867	3.609	3.252	15.1	76	0.550	1.499	6.976	0.589
3.609	4.543	4.094	23.9	80	0.550	1.345	3.951	0.379
4.543	5.720	5.153	37.9	77	0.550	1.267	2.023	0.233
5.720	7.201	6.488	60.2	89	0.550	1.281	1.345	0.157
7.201	9.065	8.168	95.3	94	0.550	1.234	0.667	0.102
9.065	11.412	10.236	136.8	80	0.550	1.282	0.199	0.065
11.412	14.367	12.985	208.2	107	0.540	1.171	0.062	0.050
14.367	18.087	16.222	318.8	138	0.526	1.201	-0.006	0.037
18.087	22.770	20.440	367.9	148	0.507	1.157	-0.042	0.033
22.770	28.666	25.669	498.1	209	0.497	1.181	-0.002	0.029
28.666	36.088	32.557	773.6	339	0.489	1.156	0.018	0.024
36.088	45.432	41.011	1306.0	567	0.490	1.157	0.012	0.018
45.432	57.196	51.592	2209.4	931	0.489	1.153	-0.003	0.014
57.196	72.005	64.800	3453.1	1508	0.490	1.153	0.014	0.011
72.005	90.649	81.104	4393.5	1858	0.489	1.150	-0.002	0.010
90.649	114.120	98.841	2447.6	1021	0.488	1.145	-0.011	0.013
114.120	143.669	118.289	171.3	63	0.453	1.141	-0.033	0.046

Table 7. K105 Star Counts.

r_{inner} arcsec	r_{outer} arcsec	r arcsec	area arcsec^2	N	f_{bkd} arcsec^{-2}	α_c	f arcsec^{-2}	
2.867	3.609	3.253	15.1	32	0.208	1.579	3.140	0.464
3.609	4.543	4.094	23.9	21	0.208	1.212	0.857	0.199
4.543	5.720	5.153	37.9	25	0.208	1.337	0.674	0.141
5.720	7.201	6.488	60.2	20	0.208	1.450	0.274	0.078
7.201	9.065	8.153	93.3	29	0.208	1.246	0.179	0.059
9.065	11.412	10.227	118.5	31	0.208	1.275	0.126	0.048
11.412	14.367	12.916	150.1	31	0.208	1.234	0.047	0.037
14.367	18.087	16.148	185.6	33	0.208	1.324	0.028	0.031
18.087	22.770	20.421	181.6	22	0.207	1.196	-0.062	0.026
22.770	28.666	25.620	279.9	57	0.176	1.142	0.057	0.027
28.666	36.088	32.671	445.1	53	0.153	1.087	-0.023	0.016
36.088	45.432	41.059	789.4	99	0.156	1.095	-0.019	0.013
45.432	57.196	51.858	1415.6	211	0.164	1.096	0.000	0.010
57.196	72.005	64.725	2788.3	464	0.170	1.081	0.010	0.008
72.005	90.649	81.585	4294.1	674	0.168	1.083	0.001	0.006
90.649	114.120	99.374	3560.9	552	0.172	1.078	-0.005	0.007
114.120	143.669	121.664	592.6	98	0.175	1.077	0.003	0.017

Table 8. K108 Star Counts.

r_{inner} arcsec	r_{outer} arcsec	r arcsec	area arcsec^2	N	f_{bkd} arcsec^{-2}	α_c	f arcsec^{-2}	
2.277	2.867	2.581	9.5	53	1.047	1.624	8.002 ±	0.845
2.867	3.609	3.252	15.2	62	1.047	1.510	5.125	0.555
3.609	4.543	4.094	23.9	59	1.047	1.315	2.204	0.333
4.543	5.720	5.153	37.9	57	1.047	1.339	0.965	0.204
5.720	7.201	6.489	60.1	64	1.047	1.354	0.394	0.136
7.201	9.065	8.169	95.3	98	1.047	1.370	0.362	0.106
9.065	11.412	10.285	151.0	130	1.047	1.251	0.030	0.076
11.412	14.367	12.888	216.9	176	1.047	1.283	-0.006	0.062
14.367	18.087	16.253	303.5	262	1.115	1.292	0.000	0.054
18.087	22.770	20.309	332.3	312	1.230	1.344	0.032	0.053
22.770	28.666	25.830	429.0	465	1.507	1.452	0.066	0.050
28.666	36.088	32.602	760.9	828	1.567	1.432	-0.009	0.038
36.088	45.432	40.977	1301.0	1464	1.570	1.405	0.011	0.029
45.432	57.196	51.692	2125.3	2358	1.562	1.404	-0.005	0.023
57.196	72.005	64.749	3279.9	3793	1.570	1.399	0.049	0.019
72.005	90.649	81.321	4464.6	4968	1.574	1.393	-0.023	0.016
90.649	114.120	98.378	2496.6	2823	1.581	1.376	-0.025	0.021
114.120	143.669	119.919	136.2	130	1.503	1.400	-0.167	0.084

Table 9. K219 Star Counts.

r_{inner} arcsec	r_{outer} arcsec	r arcsec	area arcsec^2	N	f_{bkd} arcsec^{-2}	α_c	f arcsec^{-2}	
2.867	3.609	3.252	15.2	100	0.029	1.757	11.567	0.670
3.609	4.543	4.094	23.9	88	0.029	1.634	5.986	0.398
4.543	5.720	5.154	37.9	81	0.029	1.543	3.265	0.240
5.720	7.201	6.488	60.1	69	0.029	1.467	1.654	0.140
7.201	9.065	8.168	95.3	62	0.029	1.494	0.942	0.084
9.065	11.412	10.261	147.1	54	0.029	1.414	0.490	0.050
11.412	14.367	12.961	204.5	28	0.030	1.253	0.142	0.026
14.367	18.087	16.215	320.3	27	0.032	1.213	0.070	0.016
18.087	22.770	20.456	359.2	16	0.035	1.109	0.015	0.011
22.770	28.666	25.736	479.3	21	0.041	1.058	0.005	0.010
28.666	36.088	32.598	782.9	27	0.044	1.046	-0.008	0.007
36.088	45.432	40.971	1355.1	41	0.044	1.047	-0.013	0.005
45.432	57.196	51.603	2314.9	117	0.044	1.052	0.009	0.005
57.196	72.005	64.767	3409.8	136	0.045	1.047	-0.003	0.003
72.005	90.649	81.072	4480.2	202	0.045	1.052	0.002	0.003
90.649	114.120	98.370	1987.5	89	0.047	1.059	0.001	0.005
114.120	143.669	118.414	180.8	8	0.049	1.050	-0.003	0.016

Table 10. Structural Parameters.

Cluster	r_c[a] (pc)	r_c[b] (pc)	r_c[c] (pc)	r_c[d] (pc)	r_c[e] (pc)	r_t[e] (pc)	r_h (pc)
K58	0.71	0.85	···	0.53	0.62	36	2.8
K105	···	···	···	0.18	0.34	36	2.9
K108	0.95	1.2	3.8	···	0.92	46	3.6
K219	···	···	···	···	1.82	52	4.7

Notes to Table 10.

[a]Battistini *et al.* 1982
[b]Crampton *et al.* 1985
[c]Cohen & Freeman 1991
[d]Fusi Pecci *et al.* 1994
[e]Present Study